

A Lymphatic Vessel on a Chip with Capability for Exposure to Cyclic Fluidic Flow

Parinaz Fathi,^{1,2,3} Glenn Holland,⁴ Dipanjan Pan,^{2,3} and Mandy B. Esch^{1,}*

¹Biomedical Technologies Group, Microsystems and Nanotechnology Division, Physical Measurement Laboratory, National Institute of Standards and Technology, Gaithersburg, Maryland 20899, United States

²Departments of Bioengineering, Materials Science and Engineering, and Beckman Institute, University of Illinois 61801, United States

³Mills Breast Cancer Institute, Carle Foundation Hospital, Urbana, Illinois 61801, United States

⁴Photonics and Plasmonics Group, Microsystems and Nanotechnology Division, Physical Measurement Laboratory, National Institute of Standards and Technology, Gaithersburg, Maryland 20899, United States

KEYWORDS. microfluidic, lymph nodes, lymphatic vessels, organ-chip, tissue-chip

ABSTRACT. The lymphatic system is a complex organ system that is essential in regulating the development of host immune responses. Due to the complexity of the lymphatic system and the existence of few *in vitro* models that replicate human lymphatic vessels, there is a need for a primary cell based lymphatic model that can provide a better understanding of the effects of flow

parameters, therapeutics, and other stimuli on lymphatic vessel behavior. In this report, a fluidic device models the cyclical lymphatic flow under normal and diseased conditions. The device utilizes a pumpless design, operating with gravitational forces to simulate normal conditions with a shear of 0.092 Pa (0.92 dyn/cm²) as well as disease conditions with increased shear of (0.67 Pa, 6.7 dyn/cm²). The cyclical pumping present in lymphatic vessels is replicated by applying shear stress for a period of ten seconds multiple times per minute. Primary human lymphatic endothelial cells (HLECs) cultured in the device for ten days produce less interleukin 8 (IL-8), and tumor necrosis factor alpha (TNF- α) per cell than cells cultured under static conditions. The results are consistent with previously published in vivo measurements, indicating that the fluidic device mimics conditions for IL-8 and TNF- α expression well. Data obtained with the devices also indicate that primary human lymphatic endothelial cells proliferate faster under high shear than under low shear conditions.

1. INTRODUCTION

The lymphatic system is designed to clear the body of toxins and foreign substances. It does so primarily through the circulation of lymph fluid that picks up immune cells in the lymph nodes and distributes them throughout the body.¹ The lymph-mediated immune response can be an important tool when treating cancer,²⁻⁴ but the presence of tumors close to lymph nodes can disturb lymphatic function. Tumors that grow nearby and drain into a node can metastasize there⁵⁻¹⁰ and increase the flow in lymphatic vessels. Metastatic tissue that already grows inside a lymph node can decrease lymphatic flow.¹¹ A tumor-related increase in flow causes heightened expression of ICAM-1, which can lead to additional metastatic growth,¹² and reduction of lymph flow due to a tumor causes increased expression of tumor necrosis factor alpha (TNF- α) and

interleukin 6 (IL-6),¹³ two cytokines that are known to reduce contraction and pumping in the lymphatic system.¹³ Furthermore, a correlation between TNF- α and IL-8 levels has been identified in breast cancer patients.¹⁴

Flow in human and mammalian lymph nodes is unidirectional due to a complex valving system¹⁵⁻¹⁸, ensuring that lymph travels only from the afferent to the efferent lymphatics. Lymph node shear values of up to 1.2 Pa (12 dyn/cm²) have been reported in rodents¹⁹, and computer simulations have predicted shears of up to 0.6 Pa (6 dyn/cm²) in human lymph nodes²⁰. Other studies have reported peak shear stresses of up to 0.8 Pa (8 dyn/cm²) for rodent lymph nodes^{21,22}. Under edemagenic conditions, shear stresses of up to 4 Pa (40 dyn/cm²) have been reported in rat lymphatics²³. Additionally, flow in the lymph nodes is not continuous, but rather is marked by contractile pumping. Lymphatic vessel pulsing frequencies in mice have been reported in the range of approximately five to eight contractions per minute¹³.

Because the lymphatic system is intimately involved in the immune response, which in turn can be a vital part of treating cancer²⁻⁴, human-based lymph node flow models will allow us to systematically probe the role of lymph flow on these processes. Current *in vitro* models of lymph nodes²⁴⁻²⁸ primarily use 2D cultures, and the models often utilize human dermal lymphatic or microvascular endothelial cells^{24,27,29} under low-shear conditions^{12,24}. Microfluidic tissue-chip and organ-chip models have recently gained increasing interest as potential alternatives to traditional *in vitro* culture models, allowing for more accurate recapitulation of physiologically relevant flows³⁰⁻³⁸. Here, we have developed a microfluidic device that produces a pulsatile flow pattern as seen in lymphatic vessels, and with shears that mimic healthy conditions (low shear), or disease conditions (high shear or no shear). We have used our devices to culture primary human lymphatic

endothelial cells (HLECs) for up to ten days, producing a healthy endothelium under low shear conditions, and an endothelium with elevated TNF- α and IL8 production under static conditions.

The device design uses gravity-driven flow, can be used for a wide range of shears, and uses only unidirectional flow. The use of gravity-driven flow provides the ability to obtain the desired shear stresses without the need for an active pumping mechanism. This design allows for the simultaneous operation of multiple devices, thereby reducing the cost of adopting such tissue-on-a-chip technologies. We achieved gravity-driven flow by placing our devices on periodically-rotating platforms, which were developed in-house. The use of unidirectional flow serves as a physiologically accurate mimic of flow in the lymphatic system.

2. RESULTS AND DISCUSSION

2.1 Device Design

Our microfluidic device design utilizes two halves which are connected by hemispherical reservoirs for the addition and removal of culture medium (**Figure 1A-B**). Each half of the device is composed of a larger channel to generate a high flowrate, followed by two smaller channels with reduced width and height to take advantage of conservation of mass to achieve higher flow velocities. Channel heights of 750 μm and a width of 5.5 mm were utilized for the larger channels, and heights of 350 μm and widths of 1.75 mm were utilized for the smaller channels. Flow occurs only on one side of the device at a time, and only in one direction (**Figure 1C**). When the device is rotated 180°, flow occurs on the other side of the device. To obtain unidirectional flow in the devices, we combined hemispherical inlet and outlet wells with channels of sizes that create strong capillary forces. When the

device is placed at an angle, the hemispherical inlets and outlets allow for the cell culture medium to create a pressure head in only one side of the device at any given time. While medium flows through the channel on that side, cell culture medium in the channel of the other side is held inside that channel by capillary forces. (Here, it is important to note that the surface of the inlet and outlet must be entirely free of any creases or wrinkles that could result in upward capillary flow within the reservoirs. We achieved this by using smooth marbles as PDMS molding material.) The device we developed takes advantage of capillary-based valving mechanisms, similar to previous reports.³⁹ The unidirectional flow behavior of an example device can be observed in **Supplementary Video 1** and **Figure S1**.

The shear generated within the device was calculated using:

$$\tau = \frac{6\eta u_{max}}{h} \quad (1)$$

Where u_{max} is the maximum velocity, η is the dynamic viscosity, and h is the channel height. The average velocity for the large and small channels was calculated using the volumetric flowrate measured when the device was placed at a 45° angle on the rotating platform, along with the channel dimensions. The average flowrate was determined to be 2.86 mL/min \pm 0.14 mL/min for the devices, corresponding to an average flowrate of 1.43 mL/min in the small channels. The average velocities calculated from these average flowrates were used in place of u_{max} to determine the average shear stresses. When placed at an angle of 45° on the rotating platform, the device obtains average shear stresses of 0.67 Pa (6.7 dyn/cm²) in small channels and 0.092 Pa (0.92 dyn/cm²) in larger channels. A dynamic viscosity of 1000 Pa*s was utilized for all calculations.

2.1.1. Rotating Platform and Device Fabrication

The rotating platforms (**Figure 1D**) were 3D-printed and make use of an Arduino microcontroller and basic circuitry to rotate 180° , hold the position for 10 s, and then rotate another 180° . The platform base remains stationary, while the platform rotor position can be set to angles between 0° and 90° to control the flowrates and resulting shear stresses in the device. Devices were fabricated using three layers of PDMS (**Figure 1E**). A detailed description of the fabrication process is provided in the experimental section. Photographs of the 3D-printed rotating platform and devices on the rotating platform are shown in **Figure 1F**.

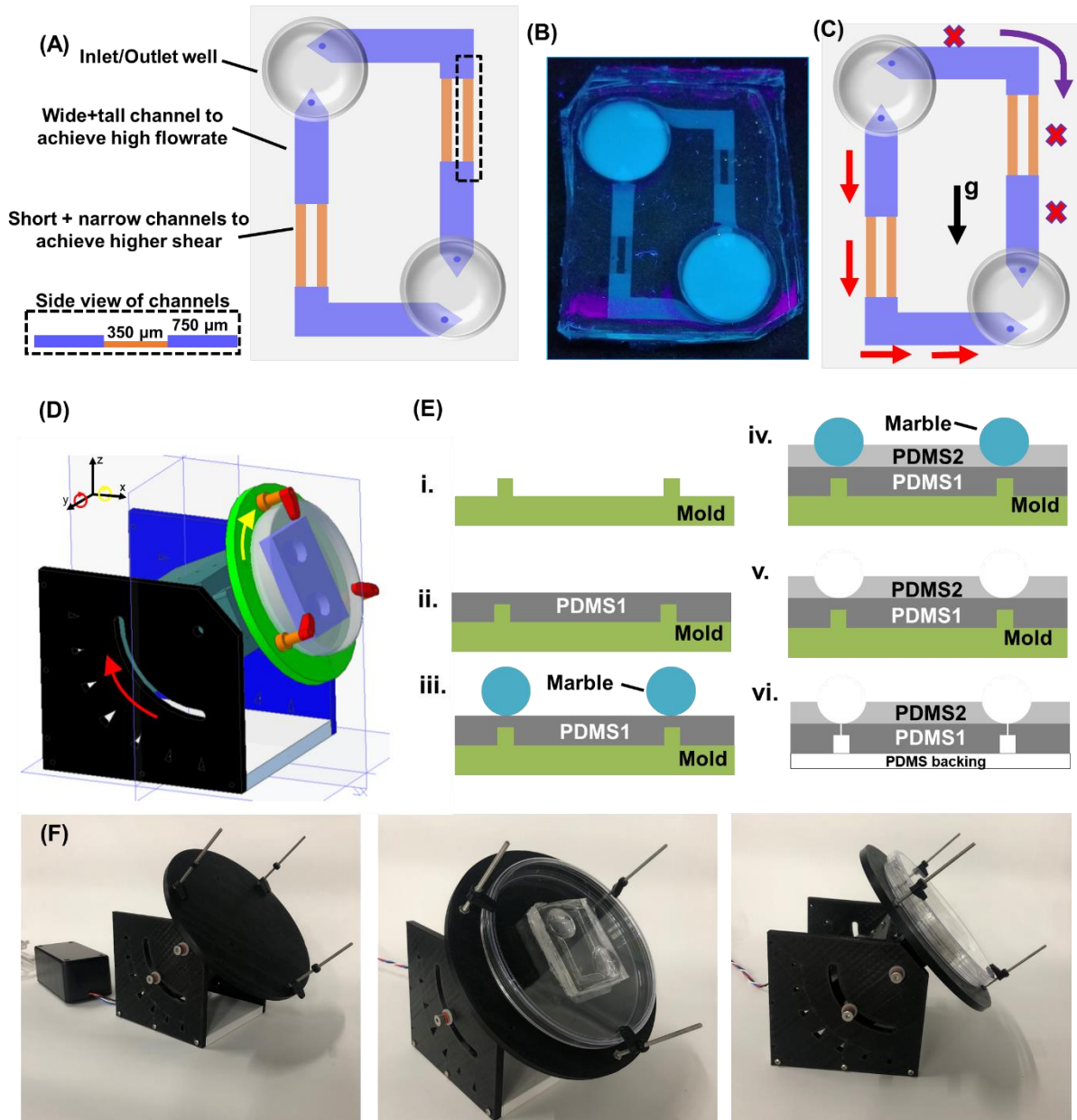


Figure 1. Device design. **(A)** A combined inlet/outlet well allows for liquid to flow from one side of the device into the other side of the device. Wide and tall channels allow the device to achieve a high flowrate and allow for the growth of cells under low-shear conditions. Shorter narrower channels allow for growth of cells under a higher shear condition. **(B)** Fabricated device filled with a solution of fluorescent molecule, visualized under a 365 nm ultraviolet lamp. **(C)** Red arrows and ‘x’ indicate presence and absence of flow respectively. Unidirectional flow is achieved by having flow on only one side of the device at a time. Purple arrow indicates direction of 180° rotation of platform to achieve flow on other side of device. g indicates gravity. **(D)** 3D model of rotating platform on which devices are placed. Red arrow indicates adjustable positioning of platform angle. Yellow arrow indicates direction of platform rotation. These two types of motion occur in different planes. **(E)** Cross-section view of device fabrication. **i.** A 3D-printed mold is obtained. **ii.** A layer of PDMS is cured onto the mold. **iii.** Marbles are placed over the desired

location of inlet and outlet wells. **iv.** A second layer of PDMS is added and cured onto the mold. **v.** The marbles are removed, retaining the well feature of the device. **vi.** The device is separated from the mold, holes are punched in the inlet and outlet wells, and the device is sealed with a PDMS backing. **(F)** Photographs of the fabricated 3D-printed platform and devices on the platform. Rotating platform without any devices (left), and with a device placed at an angle (center, right).

2.2 Long-term culture of primary human lymphatic endothelial cells.

Primary human lymphatic endothelial cells were grown in the microfluidic device for ten days. In the wider channel section, the cells experienced a shear of 0.092 Pa (0.92 dyn/cm²), and in the narrow channel section, the cells experienced a shear of 0.67 Pa (6.7 dyn/cm²). The lower shear condition mimics flow conditions expected under healthy physiologic conditions,²⁰ and the higher shear condition mimics flow conditions present when non-metastatic tumors grow nearby¹¹. Like in the human body, the shear created with our device also periodically increases and decreases. Lymphatic vessel pulsing frequencies in mice have been reported in the range of approximately five to eight contractions per minute,¹³ and each side of our device undergoes three on-off cycles per minute (each 180 degree rotation takes approximately one second and is followed by a stationary ten seconds before the next rotation).

We also cultured cells in devices under static conditions, where no shear was applied. Different to typical static cultures, however, our culture was done inside the microfluidic channel to mimic static conditions that exist in cases where the tumor growth burden at a lymph node is so large that lymphatic flow decreases below normal values as found by Proulx et al¹¹. Different to typical static cultures, this condition also implies that nutrient and waste exchange in the microfluidic vessel occurs mostly via diffusion. A summary of the approximated average flow conditions is provided in Figure 2. These values do not represent the exact flow profiles experienced within the devices, but rather approximations based on the average volumetric

flowrate measured for the devices. In reality, the exact flow profile in “on” periods would begin at a slightly higher shear value as a result of the high initial pressure head caused by the height of the medium in the inlet well. A reduction in shear would then occur steadily during the remainder of each “on” period, as a result of the decrease in pressure head caused by a reduction of medium height in the inlet well.

Cells cultured both under static and dynamic conditions were imaged with bright-field and fluorescence microscopy after five and ten days of cell culture. Confluence of cells increased with time under all conditions (**Figure 3A**), but cells under shear formed uniform monolayers without gaps between cells, while cells under static conditions did not appear to reach full confluence throughout all parts of the channels. Immunostaining of PECAM/CD31 adherens junctions (**Figure 3B**) conducted on the cell cultures confirms this finding and illustrates the development of adherens junctions throughout the cell layer under low and high shear, and in all areas populated by cells under static conditions. The images also show that shear alters the cell shapes from a rounded shape to a more elongated shape which aligns with the direction of flow. This result is consistent with what we and others have found with human umbilical vein endothelial cells grown under cyclical fluidic flow³⁹.

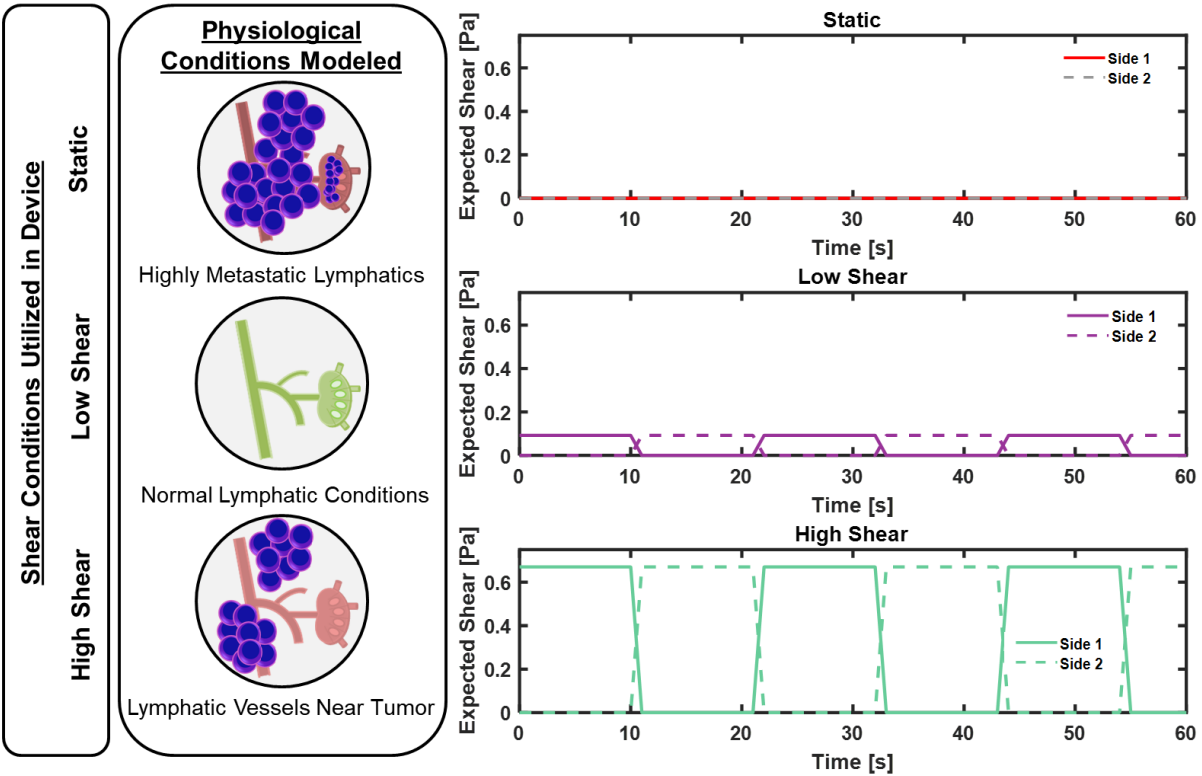


Figure 2. An approximation of average flow conditions simulated within devices. Note that the exact shear in each part of the device will experience variations in time due to the changing pressure head caused by changes in the height of medium at the inlet well as flow occurs. The use of static, low shear, and high shear conditions allows for the simulation of both normal and diseased lymphatic conditions. Expected shear profiles depict the cyclic nature of shear exerted on the devices, with each side of each device experiencing multiple on-off cycles per minute.

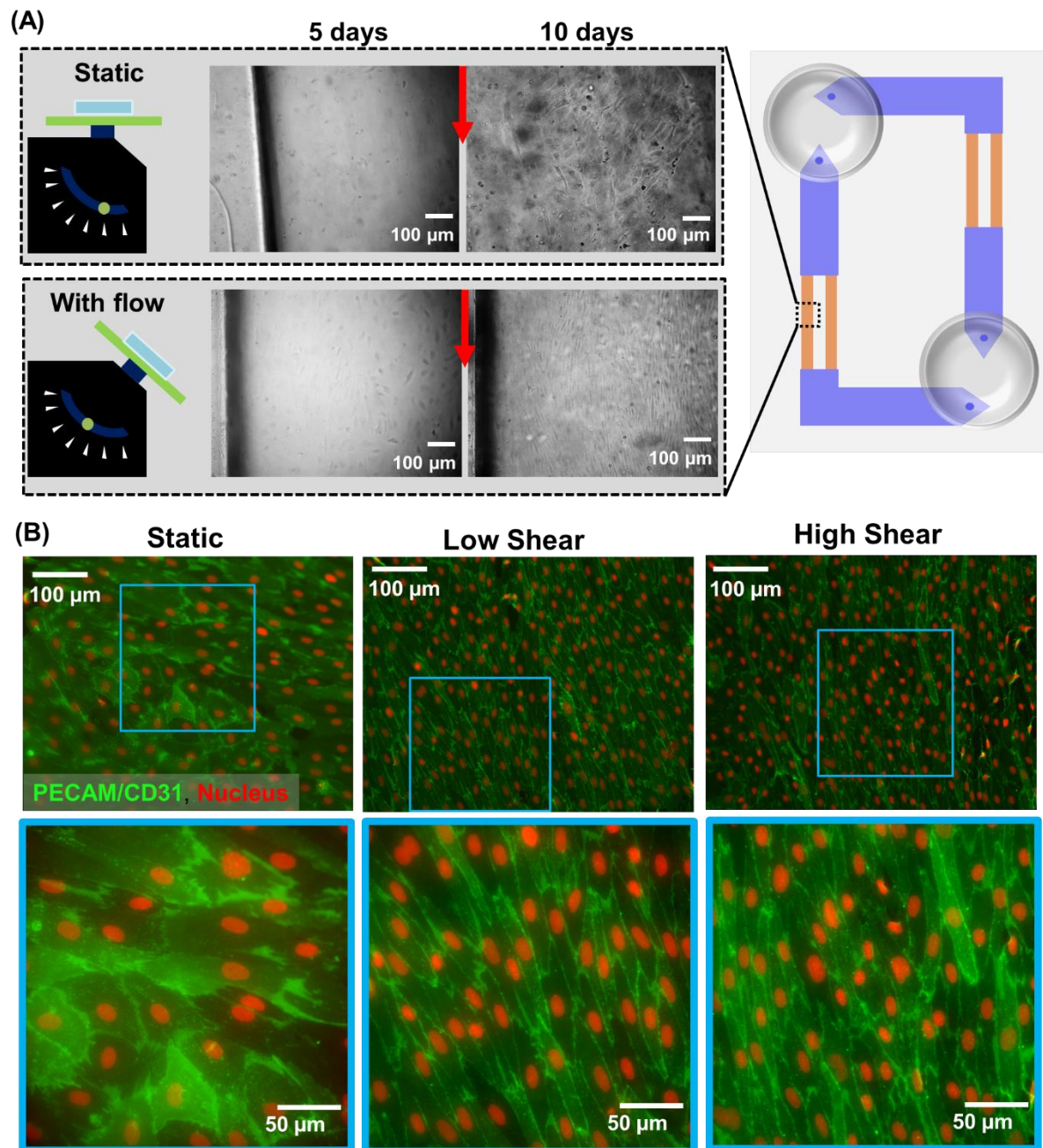


Figure 3. (A) Bright-field images 5 days and 10 days into cell culture experiment. Red arrows indicate direction of flow. Cells in static devices appear irregularly oriented, while cells in devices with flow appear to align with the direction of flow. Images are representative of observations of 8 devices (flow condition) or 7 devices (static condition). (B) PECAM/CD31 adherens junction staining of cells grown in devices for 10 days. Cells grown under all conditions continue to express PECAM/CD31 on their surfaces, while those grown under shear flow align with the direction of flow. Green color represents PECAM/CD31, red color represents the nuclear counterstain. Images are representative of observations of 3 devices for each condition (static or with flow).

2.3. Cells exposed to shear had higher viability than those grown under static conditions.

Live-dead staining determined that cells grown in both the static and flow conditions had a viability of greater than 80 % (**Figure 4A-B**). However, cells grown under high shear had a significantly higher viability than those grown under static conditions (**Figure 4B**). Future experiments with standard static cultures without use of microfluidic devices will allow for further comparison and evaluation of the viability measured with cells grown under static conditions within microfluidic devices. There was no significant difference between viability of cells in the low-shear and high-shear conditions. This confirms that the presence of flow plays an important role in delivering factors such as nutrients, intercellular signals, or mechanical cues to the cells, although these experiments do not identify the specific mechanisms by which flow affected the cells.

2.4. Cell count increased and size decreased with shear.

In addition to the changes in cell viability, the cell count per unit area increased with increases in shear (**Figure 4C**). The cell count was highest at 0.67 Pa, and lowest under static conditions. Under static conditions, the lower cell count can be partially attributed to gaps in the cell layer, but the difference in cell count between the low shear and high shear conditions was due to a difference in cell size. Indeed, under both high-shear and low-shear conditions, the monolayer was complete without uncovered surface area. In conjunction with this, cell major axis length distributions, cell minor axis length distributions, and cell area distributions were found to relate to the cell count (**Figure 4D**). The lower cell count in the static culture condition corresponded with longer major and minor axis lengths and a greater cell area, while the distribution of these measurements shifted towards lower values for each of the higher shear conditions. These findings indicate that the

application of shear, as well as the magnitude of shear applied may influence the propagation of primary human lymphatic endothelial cells.

As noted above, the presence of gaps in the cell layer under static conditions was observed. These gaps were primarily observed in the smaller channels, and are likely the result of multiple factors. First, the smaller channel height would lead to the presence of a smaller ratio of media volume to cell growth area in the smaller channels. In the presence of flow, this would not be a concern since the media would be regularly circulated throughout the device. However, under static conditions, this can lead to a restriction on the delivery of essential nutrients to cells in those channels compared to in the larger channels. Second, the distance from both the inlet and outlet wells reaches a maximum near the locations of the small channels. Under static conditions, the delivery of nutrients to the cells primarily occurs through diffusion. Since the excess medium is stored in the inlet and outlet wells, diffusion of medium must occur over a long distance in order to reach the small channels. This may also have led the cells to migrate towards the inlet and outlet wells, although further experiments would be required to confirm this. Third, the presence of flow throughout the device may encourage cell migration throughout the device, even into the smaller channels. The restriction of physicochemical cues to encourage cell migration and proliferation may have led to the occurrence of these gaps.

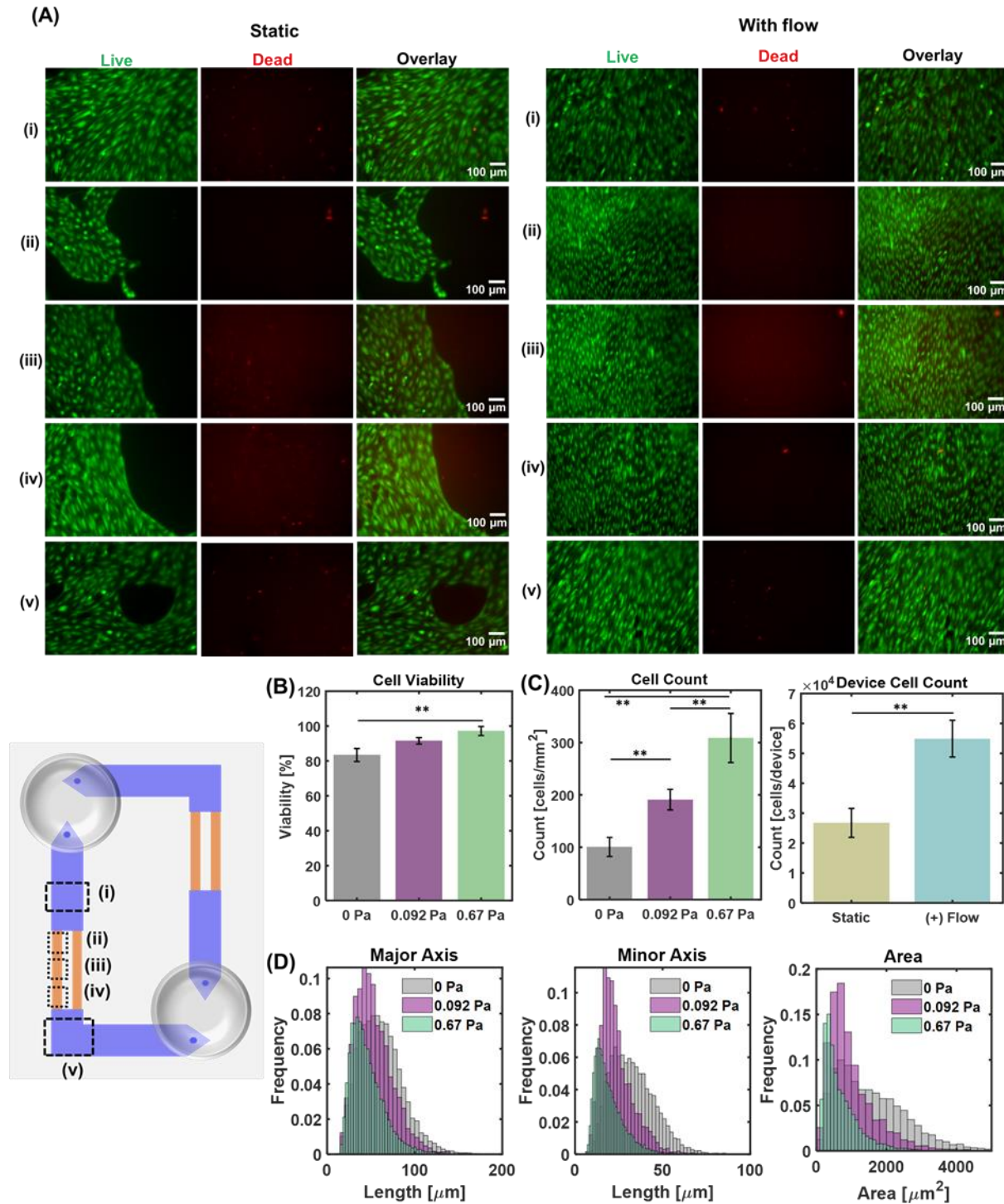


Figure 4. Live-dead images. **(A)** Representative live-dead fluorescence images of cells in devices under static conditions (left) and with flow (right). Images were taken at different positions (i-v) within the channels. The endothelial cell layer grown in devices without flow appears to be patchy, although cell viability is high. Images are representative of four devices evaluated for each

condition (static or with flow). **(B)** Cell viability calculated for each flow condition. A shear of 0.67 Pa led to significantly higher cell viability than the no-shear condition. **(C)** Cell count per unit area for each flow condition (left) and calculated cells per device (right). An increase in shear led to a direct increase in cell count. Devices with flow had a higher cell count than static devices. **(D)** Histograms of major axis length, minor axis length, and cell area calculated for cells grown under each shear condition. Cell size parameters appeared to exhibit slight decreases with increases in shear. ** indicates statistical significance with $P < 0.05$. For B-C, values are presented as an average of measurements across four devices for each condition, with error bars representing standard deviations. For D, histograms are calculated from all measurements of four devices for each condition. Full details of all calculations are provided in the Methods section.

2.5. Cells aligned with the direction of flow.

When cell directionality was quantified (**Figure 5**), the cells grown under low shear and high shear conditions were found to have an average directionality of approximately 80° to 90° , with 90° directionality indicating the cells have aligned with the direction of shear, and consequently vertically within the images. Cells grown under static conditions had an average directionality of approximately 40° to 60° , indicating that the cells had not aligned with the direction of fluidic flow. Previous studies on endothelial cell alignment with the direction of flow⁴⁰⁻⁴⁴ have primarily focused on human umbilical vein endothelial cells, and the results obtained here with human lymphatic endothelial cells confirm a similar behavior for the *in vitro* lymphatic endothelium.

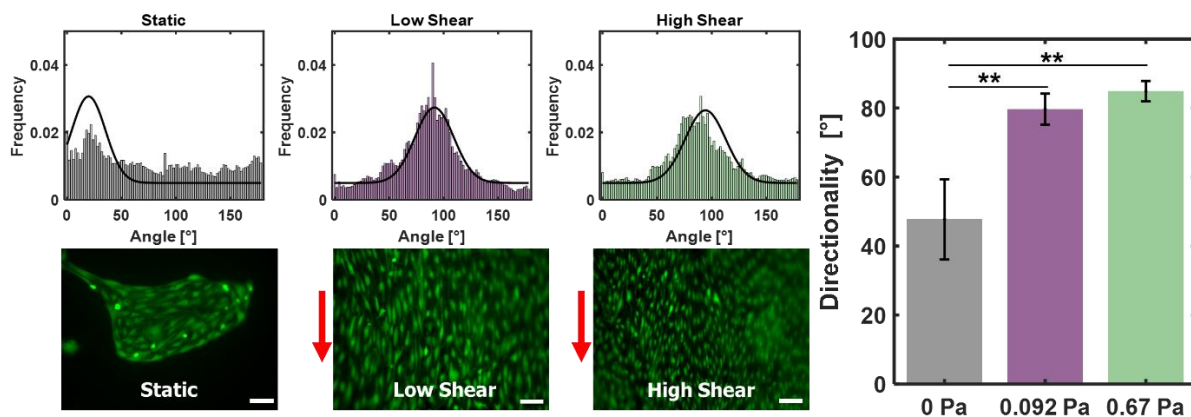


Figure 5. Cell alignment with shear flow. Red arrows indicate direction of flow. A directionality of 90° indicates complete vertical alignment. Cells grown under low or high shear were more

aligned than those grown under static conditions. ** indicates statistical significance with $P < 0.025$. Images are representative of four devices evaluated for each condition (static or with flow). values are presented as an average of measurements across four devices for each condition, with error bars representing standard deviations.

2.6. Static cultures had higher normalized TNF- α and IL-8 levels.

Medium was collected from the cell cultures daily, and ELISA assays were used to determine the levels of TNF- α and IL-8 in the medium at days 2, 4, 6, 8, and 10 (**Figure 6, Figure S2**). Taking into consideration the higher overall cell counts for devices with flow compared to static devices, normalized cytokine expression was calculated by dividing the cytokine concentrations by the final average cell count in each device (**Figure 6A-B**). This allowed us to isolate the effects of shear from the effects of overall cell density on cytokine expression. The analysis determined that the application of flow led to reduced production of IL-8 and TNF- α per endothelial cell. Using static experiments with permeable membranes, it has previously been reported that high TNF- α levels are related to high lymphatic vessel permeability^{45,46}, not unlike the disjointed endothelial cell layer of cells grown under static conditions in our device. In addition, high TNF- α expression has been linked to reduced contractility in mesenteric rat lymph nodes *in vivo*⁴⁷. In breast cancer patients, lymph node metastases have been correlated with a higher expression of TNF- α , and a correlation between TNF- α and IL-8 levels has also been demonstrated.¹⁴ Thus, our findings that static conditions within fluidic channels led to higher TNF- α levels demonstrate that our device provides a system that can be used to recapitulate the lymphatic vessel microenvironment in ways that are physiologically relatable to *in vivo* physiological conditions.

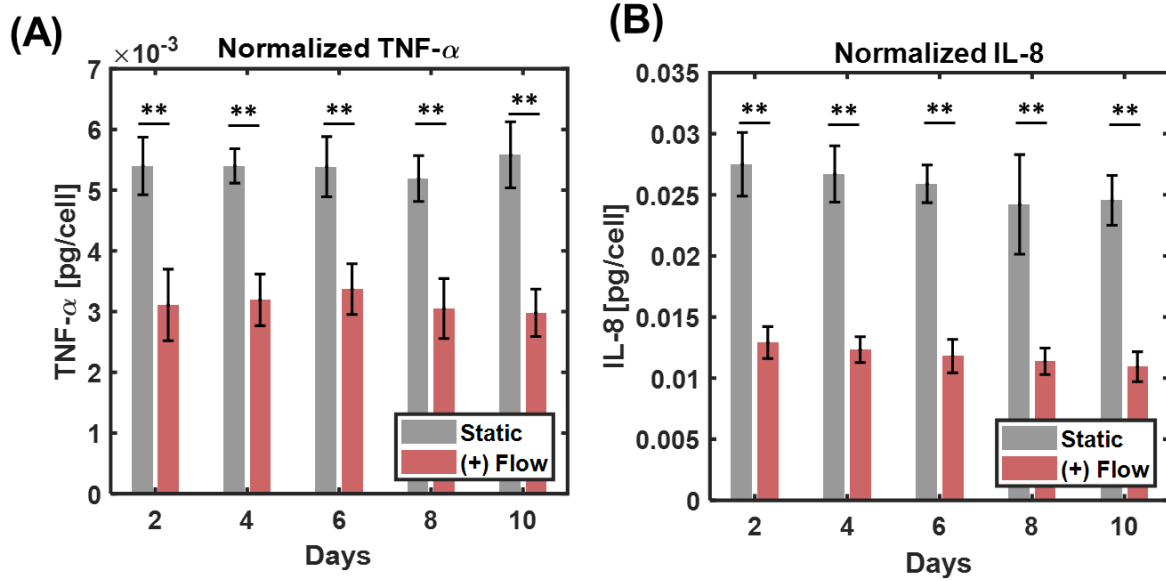


Figure 6. Cytokine expression over time. **(A)** TNF- α expression normalized by final cell count. Cells grown under static conditions had higher expression. **(B)** IL-8 expression normalized by final cell count. Cells grown under static conditions had higher expression. ** indicates statistical significance with $P < 0.001$. Values are presented as averages, with error bars representing standard deviations across 8 devices (flow condition) or 7 devices (static condition).

3. CONCLUSION

We have grown primary human lymphatic endothelial cells for ten days under fluidic flow conditions that mimic healthy and disease conditions in lymphatic vessels. Healthy conditions were simulated by applying cyclical shear of 0.092 Pa (0.92 dyn/cm²) to the cells, mimicking the natural pulsatile flow in lymphatic vessels. Disease conditions were simulated by either removing all flow from the culture, or by applying cyclical high shear (0.67 Pa, 6.7 dyn/cm²) to the cultures. Cells grown under both shear conditions formed uniform endothelial cell layers where cells developed adherens junctions and aligned with the direction of shear. Cells grown in devices under static conditions (no flow) were formed only disjointed endothelial cell layers. Cells grown under high shear had higher viability than those grown in static conditions, although viability was high (>80%) in all cases. The cell count per unit area increased with the application of shear flow,

indicating that higher shear promotes cell proliferation. Static conditions led to higher TNF- α and IL-8 levels per cell, which aligns with previous reports of the effects of lymphatic flow on cytokine expression. Overall, our study demonstrates that the developed microfluidic device can model lymphatic vessel behaviour in both healthy and diseased states. Although there are previous reports of microfluidic lymphatic models⁴⁸⁻⁵⁰, to the best of our knowledge, this is the first pumpless microfluidic model of lymphatic vessels, as well as the first microfluidic model that evaluates the effects of healthy and diseased flow conditions on primary human lymphatic endothelial cells. The developed device and rotating platform provide a versatile *in vitro* system for evaluation of lymphatic behavior under physiological shear flows. In future experiments, this device can be utilized to evaluate the interactions between cancer cells, T cells, or dendritic cells, and the lymphatic endothelial cells that line lymphatic vessels. One specific application can include the tracking of cancer cell and immune cell migration along the lymphatic vessels in order to evaluate the effects of shear flow on the rate of migration and cell viability. The migration behavior of naïve and activated T cells can also be compared. Furthermore, the application of this device design does not have to be restricted to modeling the lymphatic system. The robust device design and inexpensive 3D-printed rotating platform can be utilized for the evaluation of the effects of shear flow on any kind of primary cell or cell line that is expected to respond to flow.

4. MATERIALS AND METHODS

Materials: Devices were fabricated using polydimethylsiloxane (PDMS) (Sylgard 184) with a 10:1 base to curing agent mix ratio. Primary human lymphatic endothelial cells, endothelial cell medium, supplements, and Trypsin Neutralization solution were purchased from ScienCell Research Laboratories. Normocin was purchased from InvivoGen. The mold for device fabrication was generated in 3D drawing software and exported in a file format for 3D-printing. Molds were

3D-printed by Protolabs using WaterShed XC 11122 High-Resolution Stereolithography printed in 0.002" layers with a natural finish. Fibronectin was purchased from Sigma-Aldrich. ELISA assays for IL-8 (detection range of 1 pg/ml - 600 pg/ml, sensitivity of 1 pg/ml) and TNF- α (detection range of 30 pg/ml - 6000 pg/ml, sensitivity of 30 pg/mL) were purchased from RayBiotech. 200- μ L pipette tips used for well inlets/outlets were purchased from VWR (product 10017-098). LIVE/DEAD Cell Imaging kits, CD31 (PECAM-1) Monoclonal Antibody (Gi18), and Rabbit anti-Mouse IgG (H+L) Cross-Adsorbed Secondary Antibody, Alexa Fluor 488 were purchased from ThermoFisher Scientific. Any mention of commercial products is for information only; it does not imply recommendation or endorsement by NIST.

Cell Culture: HLECs were cultured in Endothelial Cell Medium completed with fetal bovine serum, endothelial cell growth supplement, and penicillin/streptomycin as recommended by the manufacturer. Medium was additionally supplemented with Normocin at a concentration of 0.1 mg/mL. For all experiments, medium was warmed to room temperature, per manufacturer guidelines, prior to addition to cells. Prior to culture, flasks were coated overnight with 2 μ g/cm² fibronectin. Cells were cultured in an incubator at 37 °C with a volume fraction of 5 % CO₂. For cell passaging, 5 mL Dulbecco's Phosphate Buffered Saline (DPBS) was used to rinse each T-25 flask, after which the DPBS was replaced with 1 mL of 0.25 % volume fraction trypsin, and cells were placed in the incubator for 2 min to 3 min. The trypsin was then neutralized with 1 mL trypsin neutralization solution, and cells were transferred to a centrifuge tube containing 5 mL fetal bovine serum (FBS). Cells were centrifuged at 6283 radians/min (1000 rpm) for 5 min and were resuspended in fresh medium. Each flask was split into 3 flasks during passaging.

Device Fabrication: 3D-printed mold was first taped down to a large petri dish (diameter= 14 cm). This dish was completely filled with PDMS and then cured. After curing, a 5.5 cm by 7

cm cut was used to remove the PDMS from the part of the mold containing the channel features. This prepared mold was then used for device fabrication.

For the first layer, 15 g of PDMS were added to the mold and allowed to cure at 80°C for 22 min to 25 min. To achieve the hemispherical wells in the second layer, marbles (diameter=2.54 cm) were taped onto the regions in which the hemispherical indentation was desired. 25 g PDMS were then added to the mold, and cured for 35 min. The combined first and second layer of the device was then removed from the mold, and a 1 mm biopsy punch was used to punch one hole for each inlet/outlet (two holes total per hemispherical well). In order to keep the holes open, the tips of 200 μ L pipette tips were cut to size and inserted into the 1 mm holes.

The thin bottom layer of the device was formed by partially curing 5 grams of PDMS in a 5.5 cm by 7 cm section of a 100 mm diameter petri dish. Devices were assembled immediately, and the edges of the interface between the first and third layers of the device were sealed using PDMS. To accomplish this, a toothpick was used to apply uncured PDMS around the outer edges of the device, specifically where the first and third layers of the device met. The uncured PDMS distributed itself between the already cured PDMS layers via capillary action and was then cured. This created a strong seal between the layers and prevented leakage out of the device. Cured devices were sterilized in an autoclave and cooled prior to use.

Device Preparation for Cell Seeding:

Channel Priming. Autoclaved devices were used for all experiments. Devices were transferred to a biosafety cabinet and placed in individual sterile petri dishes. Devices were kept flat and 1 mL ethanol solution with a volume fraction of 70 % was pipetted into one of the hemispherical wells for each device. The ethanol was allowed to wick into the channels, after which 1 mL of ethanol solution with a volume fraction of 70 % was added to the other

hemispherical well for each device and allowed to wick into the channels. The wells and petri dish were then completely filled with ethanol solution with a volume fraction of 70 %. Devices were incubated at room temperature for 1 h.

Fibronectin Coating. Devices were then transferred to fresh sterile petri dishes, and the ethanol solution with a volume fraction of 70 % was replaced with DPBS three times on each side of each device while the device was tilted, after which 1 mL of diluted fibronectin solution (150 μ L fibronectin, 5 mL DPBS) was added to each side of the channel and the outflowing liquid was discarded. Devices were then laid flat, their wells were filled with DPBS, and were placed in the incubator overnight. Two small segments of wet sterilized sponges were placed beside the device within each petri dish prior to device incubation. These sponges assisted in maintaining humidity to prevent solution evaporation, and were replaced every other day throughout long-term culture experiments.

Cell Seeding: Cells in passages 3 to 6 were used for all experiments in devices. Cells were allowed to grow to cover a fractional surface area of 90 % to 100 % (90 % to 100 % confluency), and were trypsinized and spun down as previously described. Each T-25 flask was resuspended in 4 mL of cell culture medium, and used for seeding one device. After overnight incubation with fibronectin, the liquid within each side of the device was replaced three times with cell culture medium while the device was tilted to allow for flow. Each side of each device was then seeded with 2 mL of the cell suspension, with the well output being saved and added back into the wells after the device was laid flat. Devices were then incubated for 2 h to allow HLECs to adhere to the channel surface. Following this, medium on each side of the device was replaced twice with fresh medium while the device was tilted. Devices were then placed horizontally, and medium in the wells were replaced with a total of 800 μ L medium per device. For experiments, devices were

either placed horizontally in the incubator (no-flow condition) or at an angle of 45° on the rotating platform (with-flow condition).

Long-term Culture of Cells in Devices:

Flow Experiments. The rotating platform angle was initially adjusted to 0°, and devices were stacked on the platform rotor, after which they were secured in place using 3D-printed fasteners built into the platform. Up to two devices at a time were placed on each platform. Platform rotation was started, and platform angle was then gently adjusted to 45°. Rotating platforms were then placed in the incubator. Experiments were conducted for 10 days, with medium collected each day and replaced with 800 µL fresh medium. Medium was stored frozen for use in ELISA assays.

No-flow Experiments. Experiments were conducted for 10 days, with medium collected each day and replaced with 800 µL fresh medium. Devices were tilted and medium was allowed to flow through the channels at least two times for each side of the device prior to medium collection. This procedure ensured that collected medium was well-mixed and that cytokines produced over the past day were evenly distributed within the device and collected medium. Similarly, after the addition of fresh medium each day, devices were tilted and medium was allowed to flow through the channels at least two times for each side of the device. This procedure ensured that the cells within channels had access to fresh medium and would not starve in nutrient-depleted medium. Media was stored frozen for use in ELISA assays.

Cell Viability Experiments. After 10 days of culture, live-dead fluorescent staining was conducted on 4 devices each for the flow and no-flow conditions. Culture medium was removed while devices were laid flat. Live and dead dye kit components were mixed and diluted in a 1:1 ratio with fresh culture medium, and added to devices while devices were tilted to allow for flow.

After devices were laid flat, 1 mL of dye-medium solution was added to each side of each device, and devices were then incubated in the dark at room temperature for 15 min to 20 min. The dye-medium solution was then replaced with DPBS for fluorescence microscopy.

The number of live and dead cells were quantified in ImageJ using the “Find Maxima” Process, and the cell viability was defined by the following equation:

$$\% \textit{Viability} = \left(\frac{\textit{number of live cells}}{\textit{number of live cells} + \textit{number of dead cells}} \right) \times 100\% \quad (2)$$

Analysis for Devices with Flow. To determine the viability under high-shear conditions, 3 images (top, middle, and bottom) were collected for each small channel (12 images per device). The number of live cells and number of dead cells were summed across all 12 images for each device. 4 devices were used for this analysis, with averages and standard deviations calculated for these 4 devices.

To determine the viability under low-shear conditions, on each side of each device one image was taken in the portion of the large channel before the small channels, and one was taken in the portion of the large channel after the small channels (4 images per device). The number of live cells and number of dead cells were summed across all 4 images for each device. 4 devices were used for this analysis, with averages and standard deviations calculated for these 4 devices.

Analysis for Devices without Flow. To determine the viability under no-flow conditions, 3 images (top, middle, and bottom) were acquired for each small channel (12 images per device), and 2 images were collected for each large channel (4 images per device). The number of live cells and number of dead cells were summed separately for the small channels and large channels in each device. The cell viability for the devices without flow was weighted based on the percentage of total channel area that was within each part of the device. This was done to prevent biasing of

the results towards cell behaviour in the smaller channels, as those channels represented a smaller percentage of the total channel but a larger number of images taken. The smaller channels represented a 13.2 % fraction of total channel area, while the larger channels represented a 86.8 % fraction of total channel area. Thus, the viability of the cells in the small channels and large channels were weighted to 13.2 % and 86.8 % of the viability for each device respectively. 4 devices were used for this analysis, with averages and standard deviations calculated for these 4 devices.

Immunostaining:

After 10 days of culture, cells were fixed and permeabilized, and were stained for PECAM/CD31 cell surface markers, with NucBlue used as the nuclear counterstain.

Fixation and Permeabilization. Cell fixation was conducted in multiple steps. Cells were first rinsed with DPBS 3 times. This was then replaced with 4 % by volume paraformaldehyde three times on each side of each device, and cells were fixed in this solution for 10 min. This was then replaced three times on each side of the device with 1 % by volume BSA in DPBS and cells were kept in this solution for 10 min. This solution was then replaced three times on each side of each device with 0.5 % by volume Triton-X solution, and cells were kept in this solution for 10 min. This was again replaced three times with 1 % by volume BSA in DPBS and cells were kept in this solution for 10 min. The wells were then filled with DPBS and devices were stored in the fridge until antibody staining was conducted.

Antibody Stain and Nuclear Counterstain. Prior to staining, devices with fixed and permeabilized cells were taken apart using a scalpel to separate the backing layer of PDMS from

the top two layers of PDMS. Samples were then incubated with a solution of 98 μL 1% BSA in DPBS, 2 μL primary antibody for approximately one hour while protected from light. After this, samples were washed three times with 1% BSA in DPBS. Samples were then incubated with a solution of 95 μL 1% BSA in DPBS, 5 μL secondary antibody for approximately one hour while protected from light, followed by washing three times with 1% BSA in DPBS. NucBlue was diluted at a concentration of two drops per mL in 1% BSA solution, and applied to the samples for 15-20 minutes while protected from light. Samples were then imaged on an inverted fluorescence microscope using the appropriate filters.

Determination of Cell Count:

Cell count per unit area. Final cell count after 10 days of culture in the devices was calculated using the live-dead fluorescence images acquired for cell viability experiments. Cell count in each image was defined as the number of live cells per image divided by the area of each image. For the cell count in devices without flow, the cell count was weighted with the percentage of total channel area that was within each part of the device (small channels vs. large channels).

Number of cells per device. The number of cells per device were calculated by multiplying the cell count per unit area for each device by the total channel area for the device. For comparison of flow and no-flow conditions, the cell count per unit area for the devices with flow was weighted by the percentage of total channel area that was within each part of the device (small channels vs. large channels).

Determination of Cell Area and Morphology: CellProfiler was utilized to determine the major axis length, minor axis length, and average area occupied by cells under the no-flow, low-shear, and high shear conditions. A modification of the “Human Cells” pipeline was used for this analysis, with a minimum diameter of 20 pixels and maximum diameter of 200 pixels. Average

values were computed for each device, and averages were taken across four devices of each type (flow, no flow). Values were weighted as described above.

Determination of Cell Directionality: Cell directionality analysis was conducted on the same fluorescence images acquired during live-dead cell staining. Cell directionality was determined in ImageJ using the Directionality function with Fourier components and 90 bins following previous reports³⁹. The average cell directionality within each device was computed by averaging the directionality values from the images for each device. Values were weighted as described above.

ELISA Assays: ELISA assays were conducted on medium collected 2, 4, 6, 8, and 10 days into the long-term device culture experiments using standard ELISA kit protocols. For IL-8 measurements, medium was diluted 1:1 with the provided assay diluent, and final IL-8 concentration was calculated with this dilution factor taken into consideration. This was done to avoid saturation of results due to the concentration of IL-8 in the samples exceeding the limit of detection. A total of 150 μ L culture medium was used in ELISA assays for each device. A sample size of 8 devices for the flow condition and 7 devices for the no-flow condition were used. To calculate the normalized cytokine expression, ELISA values for each condition (with flow, without flow) were divided by the average calculated cell count per device for each condition.

Quantification of Average Device Flowrate: To calculate the average volumetric flowrate in devices, videos of two devices were acquired when the devices were placed on an inclination of 45°. Since the flow characteristics of the two sides of each device are independent from each other, this enabled the evaluation of flow characteristics for n=4 sets of channels. Device channels were primed with ethanol, which was then replaced with cell culture medium. Once all channels were completely filled with medium, all medium within the inlet and outlet wells was removed.

Afterwards, 800 μL of medium was added to one inlet well for each device. Two to three videos were recorded for each side of each device. From the videos, the time for the complete 800 μL of medium to travel from the inlet well to the outlet well were determined. The average flowrate [$\mu\text{L/s}$] was then determined by dividing the medium volume by the travel time. The values were then converted to mL/min , and an average for each side of each device was calculated from all videos collected for that side of the device. The average and standard deviation were then calculated across all four samples. To determine the flowrate in the smaller channels, the principle of conservation of volume was used. Since flow into the channels must be equivalent to flow out of the channels, the combined flow in the small channels must be equivalent to the flow entering and exiting the device. Thus, each of the small channels can be assumed to have a volumetric flowrate equivalent to half of the total volumetric flowrate of the device.

Statistical Analysis: Statistical significance was determined using Student's t-tests assuming unequal variances. For cases in which more than one comparison was made, the Bonferroni correction was utilized to determine actual significance.

Supporting Information.

The following files are available free of charge.

Video of Unidirectional flow in device (MP4)

Images depicting unidirectional flow in device, graphs of non-normalized cytokine expression (PDF)

AUTHOR INFORMATION

Corresponding Author

*mandy.esch@nist.gov

Author Contributions

The manuscript was written through contributions of all authors. All authors have given approval to the final version of the manuscript.

Funding Sources

P. Fathi was supported by the National Physical Science Consortium and the National Institute of Standards & Technology through an NPSC graduate fellowship and by the Nadine Barrie Smith Memorial Fellowship from the Beckman Institute. Research reported in this publication was supported by the National Institute of Biomedical Imaging and Bioengineering of the National Institutes of Health under Award Number T32EB019944.

ABBREVIATIONS

HLECs, human lymphatic endothelial cells; IL-8, interleukin 8; IL-6, interleukin 6; TNF- α , tumor necrosis factor alpha; PDMS, polydimethylsiloxane; DPBS, Dulbecco's Phosphate Buffered Saline; FBS, fetal bovine serum

REFERENCES

- (1) Von Andrian, U. H.; Mempel, T. R. Homing and Cellular Traffic in Lymph Nodes. *Nat. Rev. Immunol.* **2003**, *3* (11), 867–878.
- (2) De Visser, K. E.; Eichten, A.; Coussens, L. M. Paradoxical Roles of the Immune System during Cancer Development. *Nat. Rev. Cancer* **2006**, *6* (1), 24–37.
- (3) Finn, O. J. Immuno-Oncology: Understanding the Function and Dysfunction of the Immune System in Cancer. *Ann. Oncol.* **2012**, *23* (SUPPL.8), 8–11.
- (4) Anderson, K. S.; LaBaer, J. The Sentinel within: Exploiting the Immune System for Cancer Biomarkers. *J. Proteome Res.* **2005**, *4* (4), 1123–1133.
- (5) Harisinghani, M. G.; Barentsz, J.; Hahn, P. F.; Deserno, W. M.; Tabatabaei, S.; Kaa, C. H. van de; Rosette, J. de la; Weissleder, R. Noninvasive Detection of Clinically Occult Lymph-Node Metastases in Prostate Cancer. *New Engl J. Med* **2003**, *348* (25), 2491–2499.
- (6) Maruyama, K.; Gunven, P.; Okabayashi, K.; Sasako, M.; Kinoshita, T. Lymph Node Metastases of Gastric Cancer. General Pattern in 1931 Patients. *Ann. Surg.* **1989**, *210* (5), 596–602.
- (7) Gotoda, T.; Yanagisawa, A.; Sasako, M.; Ono, H.; Nakanishi, Y.; Shimoda, T.; Kato, Y. Incidence of Lymph Node Metastasis from Early Gastric Cancer: Estimation with a Large Number of Cases at Two Large Centers. *Gastric Cancer* **2000**, *3* (4), 219–225.
- (8) Kosaka, Y.; Minatani, N.; Tanaka, Y.; Shida, A.; Kikuchi, M.; Nishimiya, H.; Waraya, M.; Katoh, H.; Sato, T.; Sengoku, N.; Tanino, H.; Yamashita, K.; Watanabe, M. Lymph Node

- Metastasis and High Serum CEA Are Important Prognostic Factors in Hormone Receptor Positive and HER2 Negative Breast Cancer. *Mol. Clin. Oncol.* **2018**, 566–574.
- (9) Chai, R.; Ma, H.; Xu, M.; Arefan, D.; Cui, X.; Liu, Y.; Zhang, L.; Wu, S.; Xu, K. Differentiating Axillary Lymph Node Metastasis in Invasive Breast Cancer Patients: A Comparison of Radiomic Signatures from Multiparametric Breast MR Sequences. *J. Magn. Reson. Imaging* **2019**, 1–8.
- (10) de Lima Vazquez, V.; Sachetto, T.; Perpetuo, N. M.; Carvalho, A. L. Prognostic Factors for Lymph Node Metastasis from Advanced Squamous Cell Carcinoma of the Skin of the Trunk and Extremities. *World J. Surg. Oncol.* **2008**, 6, 1–6.
- (11) Proulx, S. T.; Luciani, P.; Derzsi, S.; Rinderknecht, M.; Mumprecht, V.; Leroux, J.-C.; Detmar, M. Quantitative Imaging of Lymphatic Function with Liposomal Indocyanine Green. *Cancer Res.* **2010**, 70 (18), 7053–7062.
- (12) Kawai, Y.; Kaidoh, M.; Yokoyama, Y.; Ohhashi, T. Pivotal Roles of Shear Stress in the Microenvironmental Changes That Occur within Sentinel Lymph Nodes. *Cancer Sci.* **2012**, 103 (7), 1245–1252.
- (13) Aldrich, M. B.; Sevick-Muraca, E. M. Cytokines Are Systemic Effectors of Lymphatic Function in Acute Inflammation. *Cytokine* **2013**, 64 (1), 362–369.
- (14) Xu, J.; Ji, Y.-H.; Dai, Z.-J.; Ma, Y.; Ren, Y.; Wu, C.-J. IL-6, IL-8 and TNF- α Levels Correlate with Disease Stage in Breast Cancer Patients. *Adv. Clin. Exp. Med.* **2017**, 26 (3), 421–426.

- (15) Breslin, J. W. Mechanical Forces and Lymphatic Transport. *Microvasc. Res.* **2014**, *96*, 46–54.
- (16) SCHMID-SCHÖNBEIN, G. W. The Second Valve System in Lymphatics. *Lymphat. Res. Biol.* **2003**, *1* (1), 25–31.
- (17) Von Der Weid, P. Y.; Zawieja, D. C. Lymphatic Smooth Muscle: The Motor Unit of Lymph Drainage. *Int. J. Biochem. Cell Biol.* **2004**, *36* (7), 1147–1153.
- (18) Weber, E.; Sozio, F.; Gabbriellini, E.; Rossi, A. Lymphatic Vessels in Health and Disease. *Transl. Vasc. Med. Pathog. Diagnosis, Treat.* **2013**, *5* (February), 137–150.
- (19) Zawieja, D. C.; Greiner, S. T.; Dixon, J. B.; Moore, J. E.; Cote, G. L.; Gashev, A. A. Lymph Flow, Shear Stress, and Lymphocyte Velocity in Rat Mesenteric Prenodal Lymphatics. *Microcirculation* **2006**, *13* (7), 597–610.
- (20) Jafarnejad, M.; Woodruff, M. C.; Zawieja, D. C.; Carroll, M. C.; Moore, J. E. Modeling Lymph Flow and Fluid Exchange with Blood Vessels in Lymph Nodes. *Lymphat. Res. Biol.* **2015**, *13* (4), 234–247.
- (21) Mukherjee, A.; Hooks, J.; Nepiyushchikh, Z.; Dixon, J. B. Entrainment of Lymphatic Contraction to Oscillatory Flow. *Sci. Rep.* **2019**, *9* (1), 1–14.
- (22) Dixon, J. B.; Greiner, S. T.; Gashev, A. A.; Cote, G. L.; Moore, J. E.; Zawieja, D. C. Lymph Flow, Shear Stress, and Lymphocyte Velocity in Rat Mesenteric Prenodal Lymphatics. *Microcirculation* **2006**, *13* (7), 597–610.
- (23) Rahbar, E.; Akl, T.; Coté, G. L.; Moore, J. E.; Zawieja, D. C. Lymph Transport in Rat

- Mesenteric Lymphatics Experiencing Edemagenic Stress. *Microcirculation* **2014**, *21* (5), 359–367.
- (24) Pisano, M.; Triacca, V.; Barbee, K. A.; Swartz, M. A. An in Vitro Model of the Tumor-Lymphatic Microenvironment with Simultaneous Transendothelial and Luminal Flows Reveals Mechanisms of Flow Enhanced Invasion. *Integr. Biol. (United Kingdom)* **2015**, *7* (5), 525–533.
- (25) Moura Rosa, P.; Gopalakrishnan, N.; Ibrahim, H.; Haug, M.; Halaas, Ø. The Intercell Dynamics of T Cells and Dendritic Cells in a Lymph Node-on-a-Chip Flow Device. *Lab Chip* **2016**, *16* (19), 3728–3740.
- (26) Gopalakrishnan, N.; Hannam, R.; Casoni, G. P.; Barriet, D.; Ribe, J. M.; Haug, M.; Halaas. Infection and Immunity on a Chip: A Compartmentalised Microfluidic Platform to Monitor Immune Cell Behaviour in Real Time. *Lab Chip* **2015**, *15* (6), 1481–1487.
- (27) Sato, M.; Sasaki, N.; Ato, M.; Hirakawa, S.; Sato, K.; Sato, K. Microcirculation-on-a-Chip: A Microfluidic Platform for Assaying Blood-and Lymphatic-Vessel Permeability. *PLoS One* **2015**, *10* (9), 1–19.
- (28) Ross, A. E.; Belanger, M. C.; Woodroof, J. F.; Pompano, R. R. Spatially Resolved Microfluidic Stimulation of Lymphoid Tissue: Ex Vivo. *Analyst* **2017**, *142* (4), 649–659.
- (29) Jafarnejad, M.; Cromer, W. E.; Kaunas, R. R.; Zhang, S. L.; Zawieja, D. C.; Moore, J. E. Measurement of Shear Stress-Mediated Intracellular Calcium Dynamics in Human Dermal Lymphatic Endothelial Cells. *Am. J. Physiol. Circ. Physiol.* **2015**, *308* (7), H697–H706.

- (30) Nie, J.; Gao, Q.; Wang, Y.; Zeng, J.; Zhao, H.; Sun, Y.; Shen, J.; Ramezani, H.; Fu, Z.; Liu, Z.; Xiang, M.; Fu, J.; Zhao, P.; Chen, W.; He, Y. Vessel-on-a-Chip with Hydrogel-Based Microfluidics. *Small* **2018**, *14* (45), 1–14.
- (31) Hao, S.; Ha, L.; Cheng, G.; Wan, Y.; Xia, Y.; Sosnoski, D. M.; Mastro, A. M.; Zheng, S. Y. A Spontaneous 3D Bone-On-a-Chip for Bone Metastasis Study of Breast Cancer Cells. *Small* **2018**, *14* (12), 1–10.
- (32) Oliveira, M. B.; Salgado, C. L.; Song, W.; Mano, J. F. Combinatorial On-Chip Study of Miniaturized 3D Porous Scaffolds Using a Patterned Superhydrophobic Platform. *Small* **2013**, *9* (5), 768–778.
- (33) Ribas, J.; Zhang, Y. S.; Pitrez, P. R.; Leijten, J.; Miscuglio, M.; Rouwkema, J.; Dokmeci, M. R.; Nissan, X.; Ferreira, L.; Khademhosseini, A. Biomechanical Strain Exacerbates Inflammation on a Progeria-on-a-Chip Model. *Small* **2017**, *13* (15), 1–13.
- (34) Biglari, S.; Le, T. Y. L.; Tan, R. P.; Wise, S. G.; Zambon, A.; Codolo, G.; De Bernard, M.; Warkiani, M.; Schindeler, A.; Naficy, S.; Valtchev, P.; Khademhosseini, A.; Dehghani, F. Simulating Inflammation in a Wound Microenvironment Using a Dermal Wound-on-a-Chip Model. *Adv. Healthc. Mater.* **2019**, *8* (1), 1–12.
- (35) Sun, W.; Luo, Z.; Lee, J.; Kim, H. J.; Lee, K. J.; Tebon, P.; Feng, Y.; Dokmeci, M. R.; Sengupta, S.; Khademhosseini, A. Organ-on-a-Chip for Cancer and Immune Organs Modeling. *Adv. Healthc. Mater.* **2019**, *8* (4), 1–12.
- (36) Fois, C. A. M.; Le, T. Y. L.; Schindeler, A.; Naficy, S.; McClure, D. D.; Read, M. N.; Valtchev, P.; Khademhosseini, A.; Dehghani, F. Models of the Gut for Analyzing the

- Impact of Food and Drugs. *Adv. Healthc. Mater.* **2019**, *8* (21), 1–23.
- (37) Kong, M.; Lee, J.; Yazdi, I. K.; Miri, A. K.; Lin, Y. D.; Seo, J.; Zhang, Y. S.; Khademhosseini, A.; Shin, S. R. Cardiac Fibrotic Remodeling on a Chip with Dynamic Mechanical Stimulation. *Adv. Healthc. Mater.* **2019**, *8* (3), 1–13.
- (38) Suurmond, C. A. E.; Lasli, S.; van den Dolder, F. W.; Ung, A.; Kim, H. J.; Bandaru, P.; Lee, K. J.; Cho, H. J.; Ahadian, S.; Ashammakhi, N.; Dokmeci, M. R.; Lee, J.; Khademhosseini, A. In Vitro Human Liver Model of Nonalcoholic Steatohepatitis by Coculturing Hepatocytes, Endothelial Cells, and Kupffer Cells. *Adv. Healthc. Mater.* **2019**, *8* (24), 1–13.
- (39) Yang, Y.; Fathi, P.; Holland, G.; Pan, D.; Wang, N. S.; Esch, M. B. Pumpless Microfluidic Devices for Generating Healthy and Diseased Endothelia. *Lab Chip* **2019**, *19* (19), 3212–3219.
- (40) Sinha, R.; Gac, S. Le; Verdonschot, N.; Berg, A. Van Den; Koopman, B. Endothelial Cell Alignment as a Result of Anisotropic Strain and Flow Induced Shear Stress Combinations. *Nat. Publ. Gr.* **2016**, No. June, 1–12.
- (41) Eskin, S. G.; Ives, C. L.; McIntire, L. V.; Navarro, L. T. Response of Cultured Endothelial Cells to Steady Flow. *Microvasc. Res.* **1984**, *94*, 87–94.
- (42) Wang, C.; Lu, H.; Alexander, M. A Novel in Vitro Flow System for Changing Flow Direction on Endothelial Cells. *J. Biomech.* **2012**, *45* (7), 1212–1218.
- (43) Kroon, J.; Heemskerk, N.; Kalsbeek, M. J. T.; Waard, V. De; Rijssel, J. Van; Théry, M.;

- Louis, H. Saint. Flow-Induced Endothelial Cell Alignment Requires the RhoGEF Trio as a Scaffold Protein to Polarize Active Rac1 Distribution. *Mol. Biol. Cell* **2017**, *28*, 1745–1753.
- (44) Ping Ng, C.; Helm, C. E.; Swartz, M. A. Interstitial Flow Differentially Stimulates Blood and Lymphatic Endothelial Cell Morphogenesis in Vitro. *Microvasc. Res.* **2004**, *68*, 258–264.
- (45) Cromer, W. E.; Zawieja, S. D.; Tharakan, B.; Childs, E. W.; Newell, M. K.; Zawieja, D. C. The Effects of Inflammatory Cytokines on Lymphatic Endothelial Barrier Function. *Angiogenesis* **2014**, *17* (2), 395–406.
- (46) Kawai, Y.; Kaidoh, M.; Yokoyama, Y.; Ohhashi, T. Pivotal Roles of Lymphatic Endothelial Cell Layers in the Permeability to Hydrophilic Substances through Collecting Lymph Vessel Walls: Effects of Inflammatory Cytokines. *Lymphat. Res. Biol.* **2014**, *12* (3), 124–135.
- (47) Chen, Y.; Rehal, S.; Roizes, S.; Zhu, H.-L.; William, C. C.; Weid, P.-Y. von der. The Pro-Inflammatory Cytokine TNF- α Inhibits Lymphatic Pumping via Activation of the NF-KB - INOS Signaling Pathway. *Microcirculation* **2017**, *24* (3), 1–13.
- (48) Ayuso, J. M.; Gong, M. M.; Skala, M. C.; Harari, P. M.; Beebe, D. J. Human Tumor-Lymphatic Microfluidic Model Reveals Differential Conditioning of Lymphatic Vessels by Breast Cancer Cells. *Adv. Healthc. Mater.* **2020**, *9* (3), 5–12.
- (49) Luque-González, M. A.; Reis, R. L.; Kundu, S. C.; Caballero, D. Human Microcirculation-on-Chip Models in Cancer Research: Key Integration of Lymphatic and Blood Vasculatures. *Adv. Biosyst.* **2020**, *2000045*, 1–21.

- (50) Henderson, A. R.; Choi, H.; Lee, E. Blood and Lymphatic Vasculatures On-Chip Platforms and Their Applications for Organ-Specific in Vitro Modeling. *Micromachines* **2020**, *11* (2), 1–32.

TABLE OF CONTENTS GRAPHIC.

